

# Process-chain approach to the Bose-Hubbard model: Ground-state properties and phase diagram

Niklas Teichmann,<sup>\*</sup> Dennis Hinrichs, and Martin Holthaus  
*Institut für Physik, Carl von Ossietzky Universität, D-26111 Oldenburg, Germany*

André Eckardt

*ICFO-Institut de Ciències Fotòniques, Mediterranean Technology Park, E-08860 Castelldefels (Barcelona), Spain*

(Received 1 April 2009; revised manuscript received 19 May 2009; published 12 June 2009)

We carry out a perturbative analysis, of high order in the tunneling parameter, of the ground state of the homogeneous Bose-Hubbard model in the Mott insulator phase. This is made possible by a diagrammatic process-chain approach, derived from Kato's representation of the many-body perturbation series, which can be implemented numerically in a straightforward manner. We compute ground-state energies, atom-atom correlation functions, density-density correlations, and occupation number fluctuations, for one-, two-, and three-dimensional lattices with arbitrary integer filling. A phenomenological scaling behavior is found which renders the data almost independent of the filling factor. In addition, the process-chain approach is employed for calculating the boundary between the Mott insulator phase and the superfluid phase with high accuracy. We also consider systems with dimensionalities  $d > 3$ , thus monitoring the approach to the mean-field limit. The versatility of the method suggests further applications to other systems which are less well understood.

DOI: [10.1103/PhysRevB.79.224515](https://doi.org/10.1103/PhysRevB.79.224515)

PACS number(s): 67.85.Hj, 64.70.Tg, 03.75.Lm, 03.75.Hh

## I. INTRODUCTION

With the seminal experiment by Greiner *et al.*,<sup>1</sup> who observed the quantum phase transition from a Mott insulator to a superfluid<sup>2</sup> in a gas of ultracold rubidium atoms stored in a three-dimensional (3D) optical lattice, the regime of strongly interacting Bose gases has become accessible. Due to its perfectly controllable parameters, the experimental setup, as suggested by Jaksch *et al.*,<sup>3</sup> provides a fantastic testing ground for quantum many-body physics.<sup>4</sup> Meanwhile, the transition has also been observed in one-dimensional (1D) and two-dimensional (2D) optical lattices.<sup>5,6</sup> Ultracold atoms in optical lattices are described by the Bose-Hubbard model,<sup>7</sup> which incorporates two competing trends in an elementary manner: While the repulsive interaction between the atoms tends to localize the particles at individual sites of the lattice potential, tunneling between neighboring sites favors delocalization, and tends to suppress phase fluctuations.

The Bose-Hubbard model and its descendants have been intensively studied within the last years. Important techniques for monitoring its ground-state properties and the phase diagram include the mean-field ansatz,<sup>7</sup> strong-coupling expansions,<sup>8–10</sup> the quantum rotor approach,<sup>11</sup> methods using the density matrix renormalization group (DMRG),<sup>12–15</sup> and quantum Monte Carlo (QMC) simulations.<sup>16–19</sup>

In the present work we apply a recently suggested process-chain approach<sup>20</sup> to the  $d$ -dimensional homogeneous Bose-Hubbard model, in order to investigate the properties of its ground state in the Mott insulator phase for any integer filling factor  $g \geq 1$ , as well as the phase diagram for  $d \geq 2$ , by means of a high-order expansion in the tunneling parameter. To achieve this, we have turned Kato's representation of the perturbation series<sup>21</sup> into a numerically executable algorithm which handles symbolic diagrams as inputs. Order by order, each observable then is represented by a set of such diagrams, equipped with appropriate weight factors.

The paper is organized as follows: In Sec. II the Bose-Hubbard model is briefly recapitulated. Our zeroth-order

Hamiltonian contains the local on-site interaction only, while the tunneling term will be treated perturbatively. Section III introduces Kato's formulation of the perturbation series, and explains the required elements of the diagrammatic process-chain approach.<sup>20</sup> As an instructive example for this technique, we outline in some detail how to calculate the fourth-order energy correction induced by the tunneling term. We also discuss how fully correlated ground-state expectation values are accessible via the perturbational approach. In Sec. IV we present results for the ground-state energy, correlation functions, and occupation number fluctuations, as obtained for homogeneous hypercubic lattices with dimensionality  $d=1, 2$ , and  $3$ . The required diagrams are developed, and a phenomenological scaling is suggested, which makes the data almost independent of the filling factor  $g$ . Results typically are calculated up to tenth order in the tunneling parameter. For  $d=1$  and unit filling we obtain perfect agreement with the results of the high-order symbolic perturbative expansion of Damski and Zakrzewski.<sup>22</sup> We follow their instructive work to some extent in spirit, opening up the regimes of higher  $d$  for any  $g$ . The Mott insulator-to-superfluid phase transition is then discussed in Sec. V within the framework of the process-chain approach. The phase boundary is determined by invoking the method of the effective potential which provides a convenient indicator for the transition point;<sup>23,24</sup> this leads to a computational scheme which again can be expressed in terms of diagrams.<sup>25</sup> That scheme is worked out exactly in the case of infinite lattice dimensionality  $d$ , and then reproduces the well-known mean-field result. For  $d < \infty$  our data, obtained by numerically evaluating the diagrams up to some order  $\nu$ , lend themselves to a simple extrapolation procedure for  $\nu \rightarrow \infty$ . Critical parameters are computed in this manner for  $d=2$  and  $d=3$  and any filling factor  $g$ ; for  $g=1$ , they compare quite favorably to recent high-precision QMC data.<sup>18,19</sup> The last part of this Sec. V details how the mean-field prediction is approached with increasing dimensionality of the system. We close the paper with some concluding remarks and a short outlook in Sec. VI.

## II. MODEL

Ultracold atoms in optical lattices are fairly well described by a single-band Bose-Hubbard model. *Ultracold* in this context means that the thermal de Broglie wavelength is at least equal to the lattice constant, i.e., to half the wavelength of the laser radiation generating the lattice. The assumptions underlying this model, requiring that the thermal and the interaction energies be smaller than the gap between the lowest and the first excited Bloch band, are fulfilled if the lattice is sufficiently deep. Denoting the interaction energy of a pair of particles occupying the same lattice site by  $U$ , the chemical potential at site  $i$  by  $\mu_i$ , and the hopping matrix element connecting well  $i$  and well  $j$  by  $J_{ij}$ , the model takes the form

$$H = \frac{U}{2} \sum_i \hat{n}_i(\hat{n}_i - 1) - \sum_{i,j} J_{ij} \hat{a}_i^\dagger \hat{a}_j - \sum_i \mu_i \hat{n}_i. \quad (1)$$

Here  $\hat{a}_i^\dagger$  and  $\hat{a}_i$  are the bosonic creation and annihilation operators for site  $i$ , and  $\hat{n}_i = \hat{a}_i^\dagger \hat{a}_i$  is the corresponding number operator. The chemical potential  $\mu_i$  can incorporate an arbitrary confining potential, and then depends on the lattice site. By choosing appropriate hopping elements  $J_{ij}$ , longer-range or anisotropic hopping can be modeled. In this study we stick to the paradigmatically simple case with site-independent chemical potential  $\mu$  and isotropic nearest-neighbor hopping of positive strength  $J$  on a hypercubic lattice. Utilizing the interaction energy  $U$  as the energy scale of reference, the dimensionless Hamiltonian then reads as

$$H_{\text{BH}} = H_0 + H_{\text{tun}}, \quad (2)$$

where

$$H_0 = \frac{1}{2} \sum_i \hat{n}_i(\hat{n}_i - 1) - \mu/U \sum_i \hat{n}_i \quad (3)$$

is site diagonal, and

$$H_{\text{tun}} = -J/U \sum_{\langle i,j \rangle} \hat{a}_i^\dagger \hat{a}_j \quad (4)$$

describes tunneling between adjacent sites, with  $\langle i,j \rangle$  indicating that the sum is restricted to nearest neighbors. One can easily oversee two limiting cases: If the lattice is very deep, tunneling even between neighboring wells is inhibited because the tunneling parameter  $J/U$  vanishes exponentially with increasing lattice depth.<sup>26,27</sup> The sites then decouple and the Hamiltonian becomes local; one only needs to consider  $H_0$ . Minimizing the on-site energy  $\varepsilon_i = n_i(n_i - 1)/2 - n_i\mu/U$  of a system with  $J/U=0$  leads to the site-occupancies<sup>7</sup>

$$n_i = \begin{cases} 0 & \text{for } \mu/U < 0 \\ g & \text{for } g-1 < \mu/U < g, \quad 1 \leq g \in \mathbb{N}. \end{cases} \quad (5)$$

Thus, as long as the chemical potential  $\mu/U$  falls between  $g-1$  and  $g$ , at zero temperature each site is occupied by an integer number  $g=N/M$  of atoms, where  $N$  is the total number of particles and  $M$  is the number of lattice sites. Denoting the vacuum state by  $|0\rangle$ , the  $H_0$  ground state then is given by the product state

$$|\mathbf{m}\rangle = \prod_{i=1}^M \frac{(\hat{a}_i^\dagger)^g}{\sqrt{g!}} |0\rangle. \quad (6)$$

For integer  $\mu/U$  the ground state is  $2^M$ -fold degenerate. The parameter regime  $gJ/U \ll 1$  gives rise to insulating phases, because the system remains incompressible for small, but nonzero tunneling strength. A small change of the chemical potential  $\mu$  then does not lead to a change of the occupation number:  $\partial\langle \hat{n}_i \rangle / \partial\mu = 0$ .

The opposite limiting case appears when the interaction between the particles can be neglected in comparison with the kinetic energy,  $gJ/U \gg 1$ . The ground state then becomes an ideal Bose-Einstein condensate (BEC) with all particles occupying the zero-quasimomentum state of the lowest band,

$$|\mathbf{sf}\rangle = \frac{1}{\sqrt{N!}} \left( \frac{1}{\sqrt{M}} \sum_{i=1}^M \hat{a}_i^\dagger \right)^N |0\rangle. \quad (7)$$

Observe that this is an eigenstate of  $H_{\text{tun}}$ . Nonetheless, in what follows we use the site-diagonal Hamiltonian  $H_0$  and the Fock state (6) as the starting point for our perturbative analysis.

## III. KATO FORMALISM AND PROCESS-CHAIN APPROACH

For calculating corrections to the ground-state energy and further ground-state expectation values, we resort to the representation of the perturbation series given by Kato.<sup>21,28</sup> Its distinct advantage lies in the fact that it yields closed expressions for the perturbative corrections in any order, in contrast to the more familiar recursive formulation of the Rayleigh-Schrödinger perturbation series.<sup>29,30</sup>

The ground state  $|\mathbf{m}\rangle$  of the Hamiltonian  $H_0$  is a product of local Fock states with  $g$  particles sitting at each site. When this system is subjected to some perturbation  $V$ , not necessarily given by  $H_{\text{tun}}$ , the  $n$ th-order correction to its energy is given by the trace<sup>21,28</sup>

$$E_{\mathbf{m}}^{(n)} = \text{tr} \left[ \sum_{\{\alpha_\ell\}} S^{\alpha_1} V S^{\alpha_2} V S^{\alpha_3} \dots S^{\alpha_n} V S^{\alpha_{n+1}} \right], \quad (8)$$

where the sum runs over all possible sequences  $\{\alpha_\ell\}$  of  $n+1$  non-negative integers which obey the condition

$$\sum_{\ell=1}^{n+1} \alpha_\ell = n - 1. \quad (9)$$

The operators  $S^\alpha$  linking the individual perturbation events  $V$  are given by

$$S^\alpha = \begin{cases} -|\mathbf{m}\rangle\langle\mathbf{m}| & \text{for } \alpha = 0 \\ \sum_{i \neq \mathbf{m}} \frac{|i\rangle\langle i|}{(E_{\mathbf{m}}^{(0)} - E_i^{(0)})^\alpha} & \text{for } \alpha > 0 \end{cases} \quad (10)$$

with the energies  $E_{\mathbf{m}}^{(0)} = M[g(g-1)/2 - (\mu/U)g]$  and  $E_i^{(0)} = \sum_i [n_i(n_i-1)/2 - (\mu/U)n_i]$  of the unperturbed  $H_0$  eigenstates  $|\mathbf{m}\rangle$  and  $|i\rangle$ , respectively. Because these Fock states form an orthonormal basis, one easily derives

$$S^0 S^\alpha = 0 \quad \text{for } \alpha > 0,$$

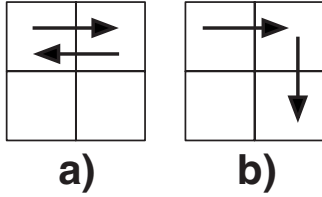


FIG. 1. Second-order tunneling processes on a lattice. While path (a) contributes, path (b) gives no contribution to the energy correction, as final and initial state do not coincide.

$$S^\alpha S^\beta = S^{\alpha+\beta} \quad \text{for } \alpha, \beta > 0. \quad (11)$$

To see how Eq. (8) works, let us consider the energy correction in second order, i.e., for  $n=2$ . The partition problem (9) then has the solutions  $\{1,0,0\}$ ,  $\{0,1,0\}$ , and  $\{0,0,1\}$ . Accordingly, one finds

$$\begin{aligned} E_{\mathbf{m}}^{(2)} &= \text{tr}[S^1 V S^0 V S^0 + S^0 V S^1 V S^0 + S^0 V S^0 V S^1] \\ &= \text{tr}[S^0 V S^1 V S^0] \\ &= \langle \mathbf{m} | V S^1 V | \mathbf{m} \rangle \\ &= \sum_{i \neq \mathbf{m}} \frac{\langle \mathbf{m} | V | i \rangle \langle i | V | \mathbf{m} \rangle}{E_{\mathbf{m}}^{(0)} - E_i^{(0)}}. \end{aligned} \quad (12)$$

In the second step, cyclic interchangeability of operators under a trace has been used, together with Eq. (11). The final expression (12) coincides exactly with the familiar textbook result provided by the Rayleigh-Schrödinger perturbation theory (see, e.g., Refs. 28 and 29), as it should.

Due to the restriction (9), in any order  $n$  at least two superscripts  $\alpha_\ell$  are equal to zero, so that the trace (8) can always be rewritten as a sum of matrix elements of the standard form  $\langle \mathbf{m} | V S^{\alpha_1} V \dots V S^{\alpha_{n-1}} V | \mathbf{m} \rangle$ . Such elements will be called *Kato terms*. We regard each Kato term as a sum over *process chains*,<sup>20</sup> leading from  $|\mathbf{m}\rangle$  back to  $|\mathbf{m}\rangle$ , with the individual processes corresponding to nonzero matrix elements  $\langle i | V | j \rangle$ .

In particular, when calculating energy corrections we identify each process with a term of  $H_{\text{tun}}$ , setting

$$V = -J/U \sum_{\langle i,j \rangle} \hat{a}_i^\dagger \hat{a}_j. \quad (13)$$

Each Kato term now can be viewed as a sum over certain chains of tunneling processes on the lattice. Because these Kato terms represent expectation values with respect to the state  $|\mathbf{m}\rangle$ , each chain has to start and to end in the state  $|\mathbf{m}\rangle$ . Thus, only closed loops of tunneling processes contribute to the energy correction. A simple example may illustrate this fact: Consider the energy correction in second order, given by Eq. (12). One then has two tunneling processes, which could take place anywhere on the lattice. But only process chains for which initial and final state both coincide with  $|\mathbf{m}\rangle$  give a contribution. This requires to tunnel back and forth, thus producing the only closed loop with two individual tunneling processes, as illustrated in Fig. 1. Such closed loops of tunneling processes will be denoted as *paths* in the following. The respective *sequence* of the individual processes, i.e., their ordering, is quite important for the evaluation of the

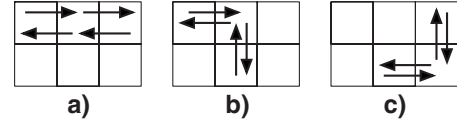


FIG. 2. Examples of topologically identical paths occurring in fourth order when calculating the energy correction. These paths are described by the same diagram.

matrix elements, as will become evident soon.

The particular perturbation (13) gives no contributions in odd order, because no closed loops can be formed with an odd number of tunneling processes on a cubic lattice. In fourth order, the general Kato terms are

$$\begin{aligned} E_{\mathbf{m}}^{(4)} &= \langle \mathbf{m} | V S^0 V S^3 V S^0 V | \mathbf{m} \rangle + 2 \langle \mathbf{m} | V S^2 V S^1 V S^0 V | \mathbf{m} \rangle \\ &\quad + \langle \mathbf{m} | V S^2 V S^0 V S^1 V | \mathbf{m} \rangle + \langle \mathbf{m} | V S^1 V S^1 V S^1 V | \mathbf{m} \rangle. \end{aligned} \quad (14)$$

The first term requires that the initial state  $|\mathbf{m}\rangle$  be recovered after the first process (numbered from right to left) because  $S^0 = -|\mathbf{m}\rangle \langle \mathbf{m}|$  occurs. With the perturbation (13) this is impossible. Hence, when treating perturbations that vanish in first order, like the tunneling events (13), one can further reduce the number of Kato terms. To the third term in Eq. (14) only chains revisiting  $|\mathbf{m}\rangle$  after two processes contribute, while evaluating the fourth term requires to take into account all those permutations of the processes forming the closed loop which do not feature the state  $|\mathbf{m}\rangle$  as an intermediate state. With four tunneling processes one can form lots of closed loops on the lattice, but as the system is homogeneous, paths which are topologically identical contribute in the same way. We subsume those topologically identical paths under a *diagram*. Examples of topologically identical paths are sketched in Fig. 2. According to the linked cluster theorem,<sup>30</sup> disconnected diagrams do not contribute. With every diagram we associate a *weight factor* which incorporates, on the one hand, the subsummation of topologically identical paths and, on the other, an additional factor of  $s^{-1}$  for a diagram visiting  $s$  lattice sites, as each of these  $s$  sites can be the “origin” of the diagram.

Thus, when calculating energy corrections the number  $\nu$  of tunneling processes agrees with the respective order  $n$  of the perturbation series, and the overall program for determining these corrections on a hypercubic lattice to a given order  $\nu$  consists of the following steps:

(i) Generate the Kato terms provided by the perturbation series (8) in  $\nu$ th order. This step is independent of the particular problem under study: Once the Kato terms are known, they can be used for all kinds of perturbative calculations. Group these terms together as far as possible, taking into account that odd orders never contribute, as there are no closed loops with an odd number of tunneling processes.

(ii) Create all paths representing a closed loop with  $\nu$  tunneling processes. Subsume topologically identical paths to diagrams, and append the correct weight factors.

(iii) For each diagram, go through all permutations of the individual processes; for each particular sequence thus obtained, determine those Kato terms which match it. Compute

TABLE I. Number of diagrams required by the energy correction for lattice dimensionality  $d$ , and number of Kato terms, vs the order  $\nu$ . If the perturbation vanishes to first order, one is left with the reduced number of Kato terms. This number is further diminished in case of the energy correction (last column) because an even number of tunneling processes has to appear between two projection operators  $S^0$ .

| $\nu$ | No. of diagrams |       |       | No. of Kato terms |         |                 |
|-------|-----------------|-------|-------|-------------------|---------|-----------------|
|       | $d=1$           | $d=2$ | $d=3$ | General           | Reduced | Energy relevant |
| 2     | 1               | 1     | 1     | 1                 | 1       | 1               |
| 4     | 2               | 3     | 3     | 4                 | 2       | 2               |
| 6     | 3               | 7     | 7     | 22                | 7       | 6               |
| 8     | 6               | 29    | 29    | 119               | 26      | 18              |
| 10    | 10              | 121   | 127   | 627               | 97      | 57              |
| 12    | 20              | 698   |       | 3216              | 357     | 175             |
| 14    | 36              |       |       | 16169             | 1297    | 546             |
| 16    | 72              |       |       | 79876             | 4628    | 1672            |

the corresponding matrix elements, including the respective energy denominators. Sum up the contributions of all sequences and all diagrams.

In high orders this procedure becomes more and more cumbersome, as the order  $\nu$  enters factorially, and both the number of diagrams and the number of Kato terms grows roughly exponentially with  $\nu$ . Table I demonstrates this for dimensionalities  $d=1, 2$ , and  $3$ . Nonetheless, a considerable advantage offered by this scheme consists in the fact that its implementation on a computer is straightforward, while a representation of the entire Hilbert space is not necessary. The strategy of determining the contributions to the perturbation series from all possible paths on the lattice then allows us to treat filling factors and dimensionalities which are difficult to reach by other approaches. In order to clarify the above steps, we give an explicit example.

### A. Example

Let us determine the fourth-order correction of the ground-state energy due to the perturbation given by  $H_{\text{tun}}$ . As the perturbation (13) is not diagonal in the Fock basis, the first and the second terms in Eq. (14) vanish. The remaining Kato terms are

$$E_{\mathbf{m}}^{(4)} = \langle \mathbf{m} | VS^2 VS^0 VS^1 V | \mathbf{m} \rangle + \langle \mathbf{m} | VS^1 VS^1 VS^1 V | \mathbf{m} \rangle. \quad (15)$$

In general, if the perturbation does not contribute to first order, the number of Kato terms can be significantly reduced,

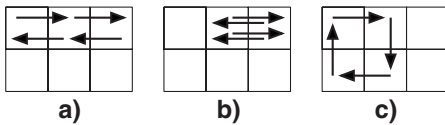


FIG. 3. Diagrams contributing in fourth order to the energy correction. We focus on diagram (a) in our example calculation. For lattice dimensionality  $d$ , the respective weight factors are (a)  $3d(2d-1)/3$ , (b)  $2d/2$ , and (c)  $2d(2d-2)/4$ .

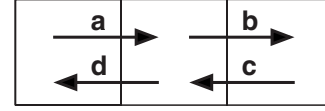


FIG. 4. Fourth-order diagram with individual tunneling processes labeled  $a, b, c$ , and  $d$ , as considered in the example calculation.

which leads to a substantial computational speedup. For calculating the energy correction one can actually reduce the number of terms still further since only an even number of tunneling processes can appear between two projection operators  $S^0$ . As shown in Table I, this approximately halves the number of terms required in tenth order. In our example, we have to evaluate the three diagrams depicted in Fig. 3, and to determine their weight factors.

We restrict ourselves to the calculation of the diagram (a) listed in Fig. 3, and denote the individual tunneling processes by  $a, b, c$ , and  $d$ , as indicated in Fig. 4. For this computation a system with three lattice sites suffices. The ground state then is represented by  $|\mathbf{m}\rangle = |g, g, g\rangle$ , with filling factor  $g$ . Out of a total number of  $4! = 24$  permutations, the first sequence to be treated here is  $(a, b, c, d)$ , leading to the following succession of intermediate states:

$$\begin{aligned} & |g, g, g\rangle \xrightarrow{a} |g-1, g+1, g\rangle \\ & \xrightarrow{b} |g-1, g, g+1\rangle \\ & \xrightarrow{c} |g-1, g+1, g\rangle \\ & \xrightarrow{d} |g, g, g\rangle. \end{aligned} \quad (16)$$

Invoking the familiar ladder relations

$$\begin{aligned} \hat{a}|n\rangle &= \sqrt{n}|n-1\rangle, \\ \hat{a}^\dagger|n\rangle &= \sqrt{n+1}|n+1\rangle \end{aligned} \quad (17)$$

for bosonic annihilation and creation operators, the factors acquired by tunneling combine to  $g(g+1)^3(J/U)^4$ . Because the initial state does not occur as an intermediate state here, this particular sequence does not match the first term in Eq. (15) so that only the second one contributes. As one particle-hole pair is present in each intermediate state, the three individual energy denominators are  $E_{\mathbf{m}}^{(0)} - E_i^{(0)} = -1$  (in multiples of the pair-interaction energy  $U$ ). The full energy denominator therefore is given by  $(-1)(-1)(-1) = -1$ . Thus, the contribution to the energy correction provided by the sequence  $(a, b, c, d)$  is

$$\Delta E_{(a,b,c,d)} = -g(g+1)^3 \left( \frac{J}{U} \right)^4. \quad (18)$$

Next, we treat the sequence  $(a, d, b, c)$ ,

$$\begin{array}{l}
 a \\
 |g, g, g\rangle \curvearrowright |g-1, g+1, g\rangle \\
 d \\
 \curvearrowleft |g, g, g\rangle \\
 b \\
 \curvearrowleft |g, g-1, g+1\rangle \\
 c \\
 \curvearrowleft |g, g, g\rangle.
 \end{array} \quad (19)$$

Here the initial state is recovered after the second tunneling process, leading to a contribution of the first term of Eq. (15), whereas the second one does not match. The prefactor due to tunneling now is  $g^2(g+1)^2(J/U)^4$ ; the energy denominator becomes  $(-1)^2(-1)=-1$ . Since  $S^0$  yields another factor of  $-1$  [see Eq. (10)], the contribution of this sequence reads as

$$\Delta E_{(a,d,b,c)} = g^2(g+1)^2 \left(\frac{J}{U}\right)^4. \quad (20)$$

In the same manner, the other 22 permutations of the processes  $a$ ,  $b$ ,  $c$ , and  $d$  have to be evaluated. Summing up all the resulting contributions, multiplying by the weight factor  $d(2d-1)$  pertaining to this particular diagram, and then adding the other two diagrams with their respective weight factors, one arrives at the total energy correction in fourth order.

### B. Ground-state expectation values

The technique introduced above also allows one to calculate expectation values  $\langle H_1 \rangle$  of observables  $H_1$  in the ground state of the homogeneous Bose-Hubbard model as expansions in the tunneling strength  $J/U$ . Considering an extended Hamiltonian

$$H = H_0 + \lambda H_{\text{tun}} + \eta H_1, \quad (21)$$

its ground-state energy generically possesses an expansion of the form

$$E = \sum_{n,m} \lambda^n \eta^m E^{(n,m)}. \quad (22)$$

Denoting the ground-state wave function of the full system (21) by  $|\psi(\lambda, \eta)\rangle$ , the Hellmann-Feynman theorem states

$$\frac{\partial}{\partial \eta} E = \langle \psi(\lambda, \eta) | \frac{\partial H}{\partial \eta} | \psi(\lambda, \eta) \rangle, \quad (23)$$

implying

$$\sum_{n,m} m \lambda^n \eta^{m-1} E^{(n,m)} = \langle \psi(\lambda, \eta) | H_1 | \psi(\lambda, \eta) \rangle \quad (24)$$

and thus resulting in

$$\sum_n E^{(n,1)} = \langle \psi(1,0) | H_1 | \psi(1,0) \rangle \equiv \langle H_1 \rangle. \quad (25)$$

This means that an implementation of Kato's perturbation series can be used for computing the desired ground-state expectation values by considering the perturbation  $V=H_{\text{tun}}+H_1$  to first order in  $H_1$ : Each process chain appear-

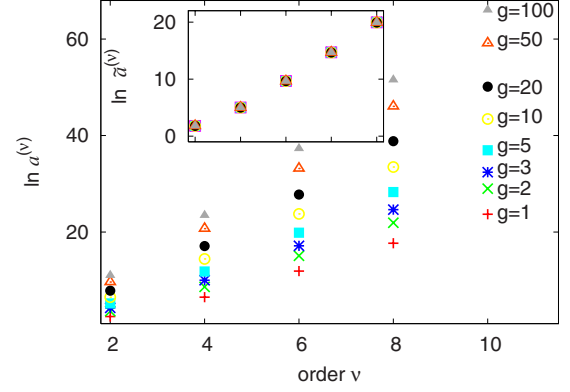


FIG. 5. (Color online) Logarithm of the coefficients  $a^{(\nu)}$  for the 3D Bose-Hubbard system with filling factors  $g=1, 2, 3, 5, 10, 20, 50, 100$ , as defined in Eq. (26). The inset shows the logarithm of the scaled coefficients [Eq. (27)], which are almost independent of  $g$ . The coefficients grow approximately exponentially with the order  $\nu$ . The results for the 2D system are qualitatively similar to these.

ing to order  $n=\nu+1$  in the perturbation series then contains  $\nu$  tunneling events described by  $H_{\text{tun}}$ , and only one process  $H_1$ .

For further details concerning the process-chain approach we refer to Ref. 20.

## IV. RESULTS

### A. Energy corrections

As the preceding example has shown, the process-chain approach in principle works for lattices of any dimensionality, with arbitrary filling factor  $g$ , but with increasing order it quickly becomes impracticable to write down the resulting terms by hand since their number proliferates rapidly, and it is unlikely that they combine to yield a simple expression. However, a numerical implementation on a computer is technically feasible and straightforward.

With our current implementation we are able to calculate energy corrections per lattice site for the one-, two-, and three-dimensional Bose-Hubbard model up to tenth order (12th order in the 1D case) in the tunneling coupling  $J/U$  for any integer filling factor  $g$  in the form

$$\frac{E - E_{\mathbf{m}}^{(0)}}{M} = - \sum_{\nu=2} a^{(\nu)}(g) \left(\frac{J}{U}\right)^{\nu}. \quad (26)$$

Our data for the 1D system with  $g=1$  agree accurately with the results reported by Damski and Zakrzewski,<sup>22</sup> who performed a high-order symbolic perturbative expansion for this particular situation. In the 2D and the 3D cases the coefficients  $a^{(\nu)}(g)$  grow to good approximation exponentially with the order  $\nu$ , as Fig. 5 demonstrates. It is of interest to observe that scaling these coefficients  $a^{(\nu)}(g)$  by factors  $\sqrt{g(g+1)}^{\nu}$  leads to data

$$\tilde{a}^{(\nu)} = \frac{a^{(\nu)}(g)}{\sqrt{g(g+1)}^{\nu}}, \quad (27)$$

which are almost independent of the filling factor, as witnessed by the inset in Fig. 5. This is intuitively intelligible, since  $\sqrt{g(g+1)}$  is a typical factor accompanying a tunneling

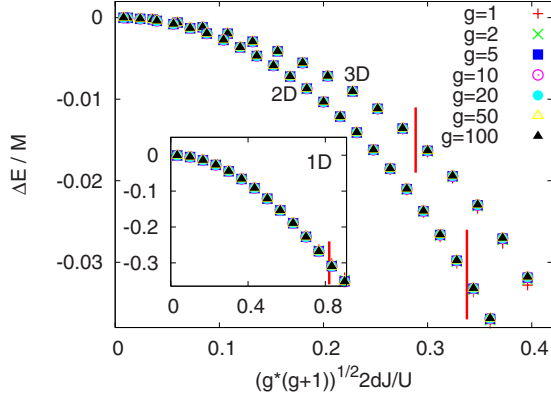


FIG. 6. (Color online) Ground-state energy correction per site  $(E - E_m^{(0)})/M$  in multiples of the pair interaction energy  $U$  for filling factors  $g=1, 2, 5, 10, 20, 50, 100$  for the 3D (upper data points), 2D (lower data points), and the 1D system (inset). Vertical lines indicate the respective critical value  $(J/U)_c$  for the Mott insulator-to-superfluid transition with  $g=1$  (see Sec. V). As a result of the scaling (29), data points for different  $g$  fall almost on top of each other.

process on a lattice which contains  $g$  particles per site on the average. Therefore, one can approximately transform the coefficients  $a^{(v)}(g_1)$  pertaining to one filling factor  $g_1$  to those referring to another factor  $g_2$ ,

$$a^{(v)}(g_1) \approx \left( \frac{g_1(g_1+1)}{g_2(g_2+1)} \right)^{v/2} a^{(v)}(g_2). \quad (28)$$

This relation even is exact in second order, whereas small deviations occur in higher orders, for which it still remains a very good estimate. Naturally, the largest deviation from this scaling behavior occurs for filling factor  $g=1$ , as will repeatedly become visible in our data.

With this observation in mind, we write

$$\frac{E - E_m^{(0)}}{M} = - \sum_{\nu=2} \tilde{a}^{(\nu)} \left( \sqrt{g(g+1)} \frac{J}{U} \right)^{\nu}. \quad (29)$$

Hence, when plotting in Fig. 6 the energy corrections as functions of  $\sqrt{g(g+1)}J/U$ , graphs originating from different filling factors  $g$  practically lie on top of each other. Of course, when keeping  $\sqrt{g(g+1)}J/U$  constant while increasing  $g$ , the zeroth-order term  $E_m^{(0)}/M = g(g-1)/2 - \mu/U$  becomes dominant, and the corrections become relatively small.

### B. Atom-atom correlation function

The atom-atom correlation function is defined by

$$C(\vec{r}_{i,j}) \equiv C_{i,j} = \langle \hat{a}_i^\dagger \hat{a}_j \rangle \quad (30)$$

with a lattice vector  $\vec{r}_{i,j}$  pointing from site  $j$  to site  $i$ . This quantity is required for computing time-of-flight absorption images, as obtained with ultracold atoms released from optical lattices.<sup>31,32</sup> Since the system is invariant under translations by integer multiples of lattice vectors,  $C_{i,j}$  depends only on  $\vec{r}_{i,j}$ , but not on the individual sites  $i$  and  $j$ . In the limit  $J/U \rightarrow 0$  the correlation function  $C_{i,j}$  vanishes for any non-

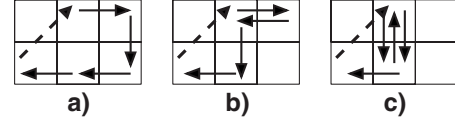


FIG. 7. Diagrams of fourth order in  $J/U$  required for calculating  $C(\vec{r})$  with  $\vec{r}=[1,1,0]$ . The associated weight factors are (a)  $12d-20$ , (b)  $12d-8$ , and (c) 4. The dashed arrow, pointing from site  $j$  to site  $i$ , describes the action of the operator (31), while the solid arrows again correspond to nearest-neighbor tunneling processes (4).

zero  $\vec{r}_{i,j}$ , whereas one has  $C_{i,j}=g$  in the BEC limit  $J/U \rightarrow \infty$ , when all particles condense into the lowest Bloch state.<sup>22</sup> The calculation of the expectation values (30) provides an example of the strategy outlined in Sec. III B, setting

$$H_1 = \hat{a}_i^\dagger \hat{a}_j. \quad (31)$$

Hence, we can employ the same implementation of the perturbation series as used for the energy correction; only the diagrams have to be adapted. Each process chain now has to contain one process (31), which has to be strictly distinguished from the nearest-neighbor tunneling processes described by  $H_{\text{tun}}$  even if  $i$  and  $j$  label adjacent sites. We therefore depict this process  $H_1$  by a dashed arrow. In Fig. 7 we display the diagrams contributing in fourth order of  $J/U$  to  $C([1,1,0])$ . Because one operator  $H_1 = \hat{a}_i^\dagger \hat{a}_j$  appears in each process chain, the required order of perturbation theory is  $n = \nu + 1$ , where  $\nu$  signals the number of ordinary tunneling processes  $H_{\text{tun}}$ , as before. When determining the weight factor of a given diagram of this kind, no division by the number of sites occurs because  $i$  and  $j$  distinguish specific sites.

We have concentrated our investigations on correlations along a line parallel to a principal axis of the lattice, and along a diagonal in a main lattice plane, as corresponding to lattice vectors

$$\begin{aligned} \vec{r}_{i,j} &= [s, 0, 0], \quad s = 1, 2, \dots, 6, \\ \vec{r}_{i,j} &= [t, t, 0], \quad t = 1, 2, 3, \end{aligned} \quad (32)$$

where  $s$  and  $t$  are given as multiples of the lattice constant. Depending on  $\vec{r}_{i,j}$ , only even or only odd orders contribute. Our current implementation is able to handle the expansion up to tenth order in  $J/U$  for dimensionalities  $d=3$  and  $d=2$ , and up to eleventh order for  $d=1$ . For the 3D system the number of the diagrams encountered is stated in Appendix A. As in the case of the energy correction, the coefficients grow approximately exponentially with the number  $\nu$  of ordinary tunneling processes. Our findings for the 1D system with unit filling ( $g=1$ ) again perfectly match the expansion reported in Ref. 22. Moreover, once again the data can be scaled such that they become almost independent of the filling factor  $g$ . To this end, we divide the correlation function by the leading density dependence, and plot  $\tilde{C}(\vec{r}_{i,j}) = C(\vec{r}_{i,j}) / \sqrt{g(g+1)}$  for fixed scaled tunneling parameter  $\sqrt{g(g+1)}J/U$  vs  $r_{i,j} = |\vec{r}_{i,j}|$ , employing the Euclidean norm. At least for sufficiently small  $\sqrt{g(g+1)}J/U$ , we then find a beautiful exponential decay of the correlations with distance, depending on the direction considered,

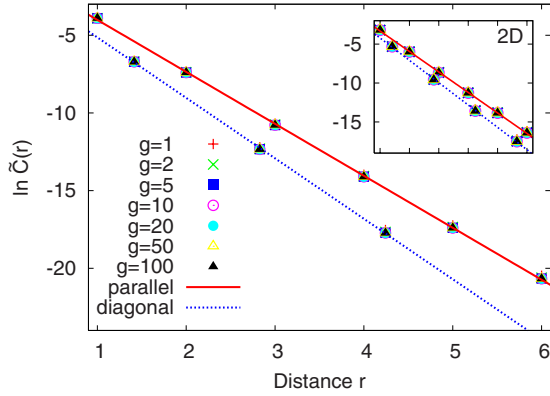


FIG. 8. (Color online) Logarithm of the scaled atom-atom correlation function  $\tilde{C}(\vec{r}) = C(\vec{r})/\sqrt{g(g+1)}$  for  $d=3$  at  $J/U=0.01/\sqrt{g(g+1)}$ , with various filling factors  $g$ . The corresponding data for  $d=2$  and  $J/U=0.02/\sqrt{g(g+1)}$  are shown in the inset. Due to the scaling, data points for different  $g$  lie almost on top of each other. The decay of the correlations is quite well described by exponential functions, as testified by the linear fits. Correlations along the diagonal (dotted lines) decay quicker than those parallel to a main axis (full lines).

$$\tilde{C}(\vec{r}_{i,j}) \propto \exp[-\alpha(J/U)r_{i,j}]. \quad (33)$$

In Fig. 8 we display logarithms of such scaled atom-atom correlations  $\tilde{C}(\vec{r}_{i,j})$  for  $d=3$  and  $d=2$ , together with linear fits. The correlations along the lattice axis are slightly larger than those along the diagonal. Figure 9 depicts  $\tilde{C}(\vec{r}_{i,j})$  for the 1D case, for three scaled tunneling parameters. As expected, lower tunneling rates lead to quicker decays of the correlations. Again the scaling works remarkably well here, mapping the data for different filling factors nearly onto each other. Such an exponential decay of 1D correlations in the regime of low tunneling rates has also been observed with DMRG methods for distances up to 20 lattice constants by Kollath *et al.*<sup>14</sup>

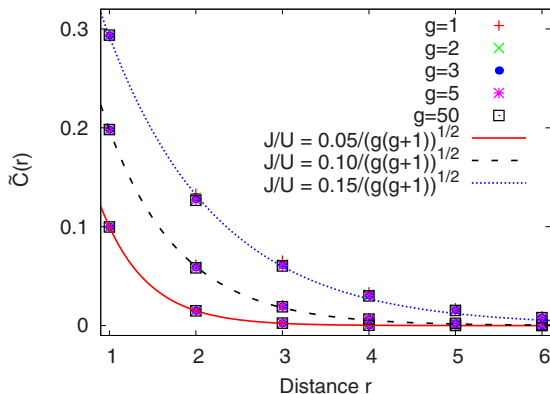


FIG. 9. (Color online) Scaled atom-atom correlation  $\tilde{C}(\vec{r}) = C(\vec{r})/\sqrt{g(g+1)}$  for the 1D system with  $g=1, 2, 3, 5, 50$  at  $J/U=0.05/\sqrt{g(g+1)}$  (full line),  $J/U=0.10/\sqrt{g(g+1)}$  (dashed line), and  $J/U=0.15/\sqrt{g(g+1)}$  (dotted line). The lines are exponential fits of the form  $\beta \exp(-\alpha r)$ , with parameters  $\alpha$  and  $\beta$  determined for  $g=4$ . With increasing tunneling parameter  $J/U$  the quality of the fit becomes less good.

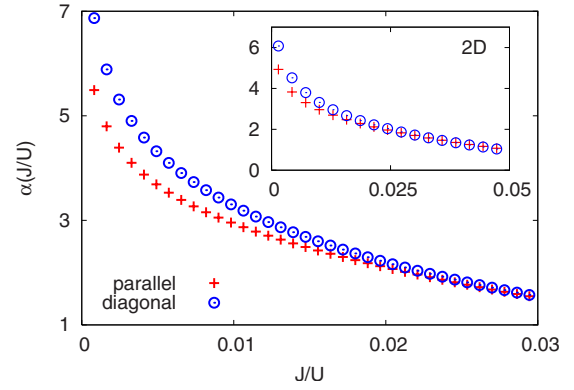


FIG. 10. (Color online) Correlation decay constants  $\alpha(J/U)$  for  $d=3$  vs tunneling coupling  $J/U$ , as determined tentatively from fits to the correlation functions. Observe that the coefficients for different directions (parallel and diagonal) converge with increasing  $(J/U)$ . The inset shows the corresponding results for  $d=2$ . All data have been computed for unit filling ( $g=1$ ).

Figure 10 shows the evolution of the two decay constants  $\alpha$  (parallel and diagonal) with increasing  $J/U$  for the 3D and the 2D systems with unit filling, determined from the slopes of linear fits to logarithmic plots similar to Fig. 8. For large  $J/U$  the data should be considered as tentative only since the quality of the fit deteriorates then. While the perturbative expansion cannot be expected to be valid beyond the critical hopping strength which marks the transition to a superfluid (with  $g=1$ , one finds  $(J/U)_c \approx 0.034$  for the 3D system and  $(J/U)_c \approx 0.059$  for the 2D case, see Refs. 9, 18, and 19 and Sec. V), and the true decay constants are supposed to vanish at that point, it is interesting to observe in Fig. 10 that the tentative data obtained for the two directions converge with increasing  $J/U$ . It might be feasible to extend the regime of validity of the perturbative approach by resumming the expansion of the correlation function; further work concerning this issue is required.

### C. Density-density correlations

Similar to the atom-atom correlation  $C(\vec{r}_{i,j})$ , we investigate the density-density correlation

$$D(\vec{r}_{i,j}) \equiv D_{i,j} = \langle \hat{n}_i \hat{n}_j \rangle. \quad (34)$$

Besides the nearest-neighbor tunneling processes  $H_{\text{tun}}$ , every process chain now contains one operator  $H_1 = \hat{n}_i \hat{n}_j$ , sketched in the diagrams by two diamonds connected by a line, as illustrated in Fig. 11. Because this process  $H_1$  does not change the particle number and leaves the state it acts on unaltered, the diagrams for  $D_{i,j}$  always contain an even number of ordinary tunneling processes, as necessary for generating closed loops, and therefore only even orders in  $J/U$  contribute. Since  $\langle \mathbf{m} | H_1 | \mathbf{m} \rangle$  does not vanish, we cannot reduce the number of Kato terms as much as was possible in the case of the energy correction and the atom-atom correlation, leaving us with higher computational effort. Moreover, the number of diagrams is larger than in the previous situations, as shown in Appendix A for  $d=3$ . We compute density-density correlations up to order 8 in the tunneling

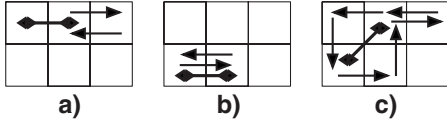


FIG. 11. Diagrams for calculating the density-density correlation  $D(\vec{r})$ . Subfigures (a) and (b) depict the second-order diagrams required for  $D([1,0,0])$ , with associated weight factors (a)  $2(2d-1)$  and (b) 1. The linked diamonds denote the operator  $\hat{n}_i\hat{n}_j$ , while arrows represent nearest-neighbor tunneling. Subfigure (c) depicts a more complicated diagram for  $D([1,1,0])$  of sixth order in  $J/U$ .

parameter  $J/U$  for the 2D and the 3D systems, and up to order ten in the 1D case.

For  $d=3$  the corrections  $\Delta D(\vec{r}_{i,j})=D(\vec{r}_{i,j})-g^2$  to the zeroth-order value  $g^2$  obtained for  $J/U=0$  are fairly small, as exemplified in Fig. 12. In the BEC limit ( $J/U \rightarrow \infty$ ), the density-density correlations again are given by  $D_{i,j}=g^2$ , assuming large systems ( $M \rightarrow \infty$ ). For small tunneling parameter  $J/U$  we observe an exponential decay of  $\Delta D(\vec{r}_{ij})$  with increasing distance  $r_{i,j}$ , as in Fig. 12. Similar to the case of the atom-atom correlations, the decay constants depend on the direction: “Diagonal” correlations tend to decay faster with distance than “parallel” ones.

#### D. Occupation number fluctuations

The squared fluctuations of the site-occupation numbers are given by the variance

$$(\Delta\hat{n})^2 = \langle\hat{n}^2\rangle - \langle\hat{n}\rangle^2. \quad (35)$$

Due to the homogeneity of the Bose-Hubbard system, this quantity is independent of the site index, and the expectation value of the number operator  $\hat{n}$  is just the filling factor  $g$ . Thus, for determining the variance (35) we need to know  $\langle\hat{n}^2\rangle$ , and therefore generate our diagrams such that besides ordinary tunneling processes  $H_{\text{tun}}$  one operator  $H_1=\hat{n}_i^2$  ap-

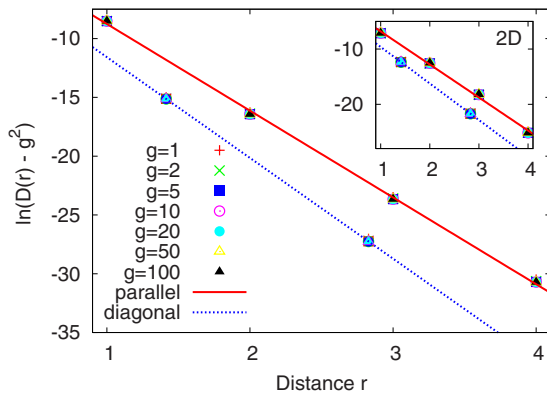


FIG. 12. (Color online) Logarithm of the correction  $\Delta D(\vec{r})=D(\vec{r})-g^2$  to the zeroth-order density-density correlation for  $d=3$  at  $J/U=0.01/\sqrt{g(g+1)}$ . Because of this scaling, data points for different filling factors  $g$  lie almost on top of each other. The decay of these corrections is quite well described by exponential functions, as emphasized by the linear fits. The inset shows data for  $d=2$  with  $J/U=0.02/\sqrt{g(g+1)}$ .

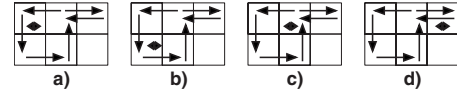


FIG. 13. Set of diagrams of sixth order in  $J/U$  for calculating  $\langle\hat{n}_i^2\rangle$ . The operator  $\hat{n}_i^2$  is marked by a diamond, which is added here in four topologically different ways to a sixth-order diagram for the energy correction. This leads to four different diagrams contributing to the perturbation series in seventh order.

pears. Because this process does not alter the system’s state, again all Kato terms have to be evaluated, as in the case of the density-density correlation. Although the diagrams now look very similar to the ones encoding the energy correction, their number is much higher when considering equal numbers  $\nu$  of tunneling processes, as revealed by Table V in Appendix A. The reason for this increase is evident in Fig. 13: The topology of the diagrams becomes more complex by introducing the additional operator  $\hat{n}_i^2$ , depicted by a diamond at site  $i$ . In the example shown in Fig. 13, one diagram contributing in sixth order of the tunneling parameter  $J/U$  to the energy correction gives rise to four different diagrams for the calculation of  $\langle\hat{n}^2\rangle$ .

We were able to determine the expansion for  $\langle\hat{n}^2\rangle$  up to order ten in the tunneling parameter  $J/U$  for dimensionalities  $d=1, 2$ , and 3. The number fluctuation  $\Delta\hat{n}$  grows approximately linearly with  $J/U$  for  $J/U < (J/U)_c$ , and our scaling for different filling factors once more works very well in this parameter regime, as demonstrated in Fig. 14. Since the critical value  $(J/U)_c$  for the Mott insulator-to-superfluid transition is roughly proportional to  $1/g$ , this implies that the relative fluctuation  $\Delta\hat{n}/\langle\hat{n}\rangle$  behaves like  $1/g$  close to the transition point. At  $(J/U)_c$  we find  $\Delta\hat{n} \approx 1/2d$ . In the superfluid regime, where the expansion in  $J/U$  is no longer valid, the fluctuation  $\Delta\hat{n}$  eventually approaches the value  $\sqrt{g}$ .

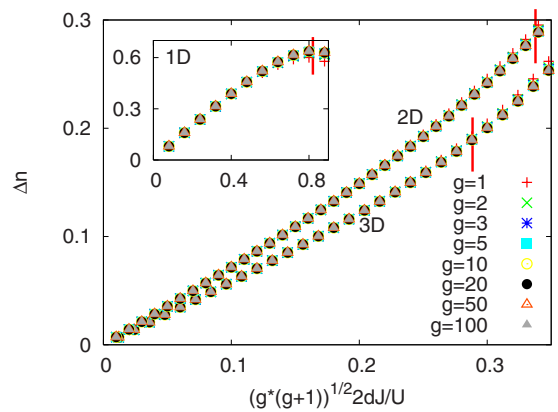


FIG. 14. (Color online) Occupation number fluctuations  $\Delta\hat{n}$  for filling factors  $g=1, 2, 3, 5, 10, 20, 50$ , and 100 for the 3D (lower data points), the 2D (upper data points), and the 1D system (inset). Vertical lines mark the critical hopping strength  $(J/U)_c$  for the Mott insulator-to-superfluid transition with unit filling. Plotted vs the scaled parameter  $2d\sqrt{g(g+1)}J/U$ , data points for different filling factors fall onto each other. For low hopping strength, the fluctuations grow linearly with  $J/U$ .

## V. MOTT-SUPERFLUID PHASE TRANSITION

A further fruitful application of the diagrammatic many-body perturbation theory based on Kato's series (8) consists in the accurate determination of the boundary between the Mott phase and the superfluid phase for the homogeneous Bose-Hubbard model.<sup>25</sup> Qualitatively, the phase diagram of the Bose-Hubbard model has been understood since the late eighties.<sup>7</sup> More quantitatively, it has been intensely studied, e.g., by means of the strong-coupling expansion conducted by Monien and co-workers<sup>8,9</sup> in one, two, and three dimensions. Recently, the quantum Monte Carlo analysis by Capogrosso-Sansone *et al.*<sup>18,19</sup> has provided quasi-exact values for  $g=1$ . In one dimension, fairly large systems even including a confining trap potential can be treated with DMRG techniques.<sup>12-15</sup> But so far, especially for dimensionalities  $d > 1$  it has remained hard to obtain precise results for filling factors well above  $g=1$ . Our approach is able to fill this gap.

### A. Method of effective potential

For locating the parameters  $(J/U)_c$  marking the quantum phase transition, we employ the method of the effective potential,<sup>23</sup> in the formulation recently given by dos Santos and Pelster.<sup>24</sup> To begin with, one adds spatially constant source and drain terms to the Bose-Hubbard Hamiltonian (2) such that particles are created and annihilated with uniform strengths  $\eta$  and  $\eta^*$  at each site,

$$\tilde{H}_{\text{BH}}(\eta, \eta^*) = H_0 + H_{\text{tun}} + \sum_i (\eta^* \hat{a}_i + \eta \hat{a}_i^\dagger). \quad (36)$$

Since our considerations apply for any fixed value of the chemical potential, we do not explicitly indicate the dependence on  $\mu/U$  in the following. We now define the grand canonical free energy at zero temperature,

$$F(J/U, \eta, \eta^*) = \langle \tilde{H}_{\text{BH}} \rangle_\eta \quad (37)$$

as the ground-state expectation value of the full Hamiltonian (36) for finite source strength, and expand this expression into a power series in  $\eta$  and  $\eta^*$ ,

$$F(J/U, \eta, \eta^*) = M \left( f_0(J/U) + \sum_{n=1}^{\infty} c_{2n}(J/U) |\eta|^{2n} \right). \quad (38)$$

The appearance of only powers of  $|\eta|^2$  reflects the fact that the free energy does not depend on the phases of  $\eta$  and  $\eta^*$ . The intensive quantity  $f_0$  denotes the free energy per lattice site in the absence of the sources. The coefficients appearing in the above expansion, in their turn, are expanded into power series in the hopping strength  $J/U$ , giving

$$c_{2n}(J/U) = \sum_{\nu=0}^{\infty} \alpha_{2n}^{(\nu)}(J/U)^\nu. \quad (39)$$

Whether the system is a Mott insulator or a superfluid is determined by its reaction to the sources. Hence, we introduce the functions

$$\psi(\eta, \eta^*) = \frac{1}{M} \frac{\partial F}{\partial \eta} = \langle \hat{a}_i \rangle_\eta,$$

$$\psi^*(\eta, \eta^*) = \frac{1}{M} \frac{\partial F}{\partial \eta^*} = \langle \hat{a}_i^\dagger \rangle_\eta, \quad (40)$$

where the respective second equalities are consequences of the Hellmann-Feynman theorem. Assuming the invertibility of these functions, we then perform a Legendre transformation from  $F$  to a function  $\Gamma$  depending on  $J/U$ ,  $\psi$ , and  $\psi^*$  as independent variables,

$$\Gamma(J/U, \psi, \psi^*) = F/M - \psi^* \eta - \psi \eta^*. \quad (41)$$

From Eqs. (40) and (38) one obtains

$$\psi(\eta, \eta^*) = c_2 \eta + 2c_4 |\eta|^2 \eta + \mathcal{O}(\eta^5),$$

$$\psi^*(\eta, \eta^*) = c_2 \eta^* + 2c_4 |\eta|^2 \eta^* + \mathcal{O}(\eta^5). \quad (42)$$

Inverting these relations and inserting into Eq. (41), one arrives at an expansion of  $\Gamma$  in powers of  $|\psi|^2$ ,

$$\Gamma(J/U, \psi, \psi^*) = f_0 - \frac{1}{c_2} |\psi|^2 + \frac{c_4}{c_2^2} |\psi|^4 + \mathcal{O}(|\psi|^6). \quad (43)$$

Because  $\eta$  and  $\psi^*$ , as well as  $\eta^*$  and  $\psi$ , constitute Legendre pairs, one also has the identities

$$\frac{\partial \Gamma}{\partial \psi^*} = -\eta \quad \text{and} \quad \frac{\partial \Gamma}{\partial \psi} = -\eta^*. \quad (44)$$

Now the original Bose-Hubbard system (2) is recovered from the extended system (36) by setting  $\eta = \eta^* = 0$ . Hence Eq. (44) implies that the system adopts that value  $\psi_0$  which renders  $\Gamma$  stationary. This is akin to a mechanical system adopting a configuration in which its potential is stationary, signaling the absence of external forces, and thus motivates to dub  $\Gamma$  as an ‘‘effective potential.’’

Unless  $\mu/U$  is integer, one finds  $c_2 < 0$  for sufficiently small  $J/U$ , whereas  $c_4 > 0$  (see Appendix B) so that one has  $\psi_0 = 0$ ; this is characteristic for the Mott phase. Upon increasing  $J/U$ , the order parameter  $\psi_0$  takes on a nonzero value when the system enters the superfluid phase, indicating long-range phase coherence. Hence, for any given value of the chemical potential the phase boundary  $(J/U)_{\text{pb}}$  is determined by that  $J/U$  for which the minimum of the expression (43) starts to deviate from  $|\psi_0|^2 = 0$ . Evidently, this occurs when the coefficient  $-1/c_2$  of  $|\psi|^2$  vanishes. We point out that  $c_2$  can be regarded as a susceptibility<sup>33</sup>  $\chi$ , being the derivative of the function  $\psi(\eta, \eta^*)$  with respect to the source  $\eta$ ,

$$\chi = \left( \frac{\partial \psi}{\partial \eta} \right)_{\eta=0} = c_2. \quad (45)$$

In effect, one has to identify that hopping parameter  $J/U$  for which the susceptibility  $c_2$  diverges; this divergence marks the quantum phase transition.

In order to compute  $c_2$  by means of the process-chain approach, we add the perturbation

$$V = -J/U \sum_{\langle i,j \rangle} \hat{a}_i^\dagger \hat{a}_j + \sum_i (\eta^* \hat{a}_i + \eta \hat{a}_i^\dagger) \quad (46)$$

to the zeroth-order Hamiltonian  $H_0$ , as implied by the extended system (36). Since  $c_2$  is the coefficient of  $|\eta|^2$  in

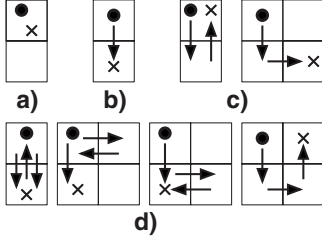


FIG. 15. Diagrams for determining  $c_2$  up to order 3 in the tunneling parameter  $J/U$ . Subfigure (a) shows the zeroth-order diagram with creation ( $\bullet$ ) and annihilation ( $\times$ ) taking place at the same lattice site, and weight factor 1. In (b) we depict the only first-order diagram; its weight factor is  $2d$ . The second-order diagrams in subfigure (c) have weight factors  $2d$  and  $2d(2d-1)$ . The weights of the third-order diagrams in (d) are (from left to right)  $2d$ ,  $2d(2d-1)$ ,  $2d(2d-1)$ , and  $2d(2d-1)^2$ . The *one-way diagrams*, which acquire the largest weights for high dimensionality, are diagrams (a) and (b), the second diagram in (c), and the last diagram in (d).

Eq. (38), it follows by comparison of coefficients with Kato's series (8) that only chains containing one creation process ( $\eta \hat{a}_i^\dagger$ ) and one annihilation process ( $\eta^* \hat{a}_j$ ) contribute to  $c_2$ . We adjust our diagrams by introducing a creation process, symbolized by a dot ( $\bullet$ ), and an annihilation process, indicated by a cross ( $\times$ ). Since the operations of creation and annihilation alter the particle number, the tunneling processes do not need to form closed loops here, in contrast to the cases examined before. This leads to contributions in even *and* odd orders of  $J/U$ . For constructing the diagrams with a specified number  $\nu$  of tunneling processes, and for appending the correct weight factors, we generate all paths from an initial site to any other site which can be reached with  $\nu$  nearest-neighbor tunneling events. The number of such paths behaves like  $(2d)^\nu$ , which is to a good approximation equal to the sum of all weight factors. As examples for the emerging diagrams, the first orders  $\nu=0, 1, 2$ , and  $3$  in the tunneling parameter  $J/U$  are visualized in Fig. 15.

Table II, which lists the number of diagrams for the 2D and the 3D system, shows that these numbers remain equal for both cases up to order  $\nu=7$  (the weight factors, of course, do depend on the lattice dimensionality). The first difference occurs in eighth order in the tunneling parameter because with eight tunneling processes it becomes possible to construct diagrams which connect more than four nearest neighbors on a hypercubic lattice. By analogy, the first difference in the number of diagrams between the 3D and the 4D model occurs for  $\nu=12$ .

TABLE II. Number of diagrams to be evaluated when calculating the phase boundary for the 2D and the 3D Bose-Hubbard model to  $\nu$ th order in the hopping parameter  $J/U$ , corresponding to the order  $\nu+2$  of Kato's perturbation series.

| $\nu$ | 0 | 1 | 2 | 3 | 4  | 5  | 6  | 7   | 8   | 9   | 10   |
|-------|---|---|---|---|----|----|----|-----|-----|-----|------|
| $d=2$ | 1 | 1 | 2 | 4 | 10 | 22 | 58 | 140 | 390 | 988 | 2815 |
| $d=3$ | 1 | 1 | 2 | 4 | 10 | 22 | 58 | 140 | 394 |     |      |

## B. Mean-field limit

For high dimensionality  $d$  the *one-way diagrams*, which avoid "back and forth tunneling" (see Fig. 15), dominate the contributions because their weight factors go with  $(2d)^\nu$  to leading power of  $d$ , whereas all other diagrams contribute with lower powers. Therefore, in the limit of large dimensionality in each order  $\nu$  *only* the one-way diagram has to be taken into account, all others possessing negligible weight factors then. These one-way diagrams can easily be evaluated analytically in every given order. Since they are one-particle reducible, they factorize into their one-particle irreducible parts as follows:<sup>24,34</sup>

$$\begin{aligned}
 \bullet \times &= (-1)^0 (\bullet \times)^1, \\
 \bullet \rightarrow \times &= (-1)^1 (\bullet \times)^2, \\
 \bullet \rightarrow \rightarrow \times &= (-1)^2 (\bullet \times)^3, \\
 &\vdots \\
 \bullet (\rightarrow)^\nu \times &= (-1)^\nu (\bullet \times)^{\nu+1}.
 \end{aligned} \tag{47}$$

Identifying the zeroth-order term ( $\bullet \times$ ) with  $\alpha_2^{(0)}$ , and accounting for the factor  $2d$  which counts the possible directions on a  $d$ -dimensional hypercubic lattice, the representation (39) of the susceptibility takes the form

$$c_2 = \alpha_2^{(0)} \sum_{\nu=0}^{\infty} (-2d\alpha_2^{(0)})^\nu (J/U)^\nu. \tag{48}$$

Because this series is geometric, its radius of convergence, and hence the phase boundary, can be immediately read off from the relation

$$-2d\alpha_2^{(0)}(J/U)_{\text{pb}} = 1. \tag{49}$$

Therefore, it only remains to compute  $\alpha_2^{(0)}$  by evaluating the diagram  $\bullet \times$ . This gives rise to two permutations, which we write as  $(\times, \bullet)$  and  $(\bullet, \times)$ : Either the creation process precedes that of annihilation, or vice versa. The only relevant Kato term now is  $\langle \mathbf{m} | V S^1 V | \mathbf{m} \rangle$ ; the respective energy denominators enforced by the linking operator  $S^1$  are  $\Delta E_{\text{particle}} = E_{\mathbf{m}}^{(0)} - E_{\text{particle}} = \mu/U - g$  for an extra particle, and  $\Delta E_{\text{hole}} = E_{\mathbf{m}}^{(0)} - E_{\text{hole}} = -\mu/U + g - 1$  for an extra hole. Thus, the two contributions figure as

$$(\times, \bullet): \frac{1}{\sqrt{g+1} \Delta E_{\text{particle}} \sqrt{g+1}} = \frac{g+1}{\mu/U - g},$$

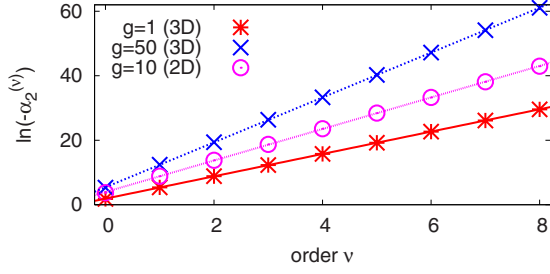


FIG. 16. (Color online) Logarithm of the coefficients  $-\alpha_2^{(\nu)}$ , obtained with filling factors  $g=1$  and  $50$  for the 3D model, and with  $g=10$  for the 2D case.

$$(\bullet, \times): \sqrt{g} \frac{1}{\Delta E_{\text{hole}}} \sqrt{g} = \frac{g}{-\mu/U + g - 1}.$$

Combining them yields

$$\alpha_2^{(0)} = -\frac{\mu/U + 1}{(\mu/U - g + 1)(g - \mu/U)}. \quad (50)$$

Putting everything together, the phase boundary in the limit of infinite dimensionality, as determined from the radius of convergence of the series (48), is given by

$$2d \left( \frac{J}{U} \right)_{\text{pb}} = \frac{(\mu/U - g + 1)(g - \mu/U)}{\mu/U + 1}, \quad (51)$$

which agrees exactly with the result of the mean-field calculation by Fisher *et al.*<sup>7</sup> This not only clarifies why the mean-field limit coincides with that of infinite dimensionality, but also gives a vivid illustration of our general approach.

### C. Results for lower dimensions

For lattice dimensionalities  $d=2$  and  $d=3$ , we have computed the (negative) coefficients  $\alpha_2^{(\nu)}$  up to order  $\nu=8$ . Again, these coefficients grow to good approximation exponentially with the number  $\nu$  of tunneling processes taken into account, as illustrated in Fig. 16 for filling factors  $g=1, 50$  ( $d=3$ ), and  $10$  ( $d=2$ ). Data for other filling factors behave similarly.

In the case of infinite dimensionality, the ratio  $\alpha_2^{(\nu-1)}/\alpha_2^{(\nu)}$  stays constant, and directly yields the phase boundary. In contrast, for finite  $d$  this ratio still changes slightly with increasing  $\nu$ . We therefore make use of a simple extrapolation scheme, based on d'Alembert's ratio test:<sup>35</sup> The radius  $r$  of convergence of a power series  $s = \sum_{\nu=0}^{\infty} b^{(\nu)} z^{\nu}$  is given by

$$r = \lim_{\nu \rightarrow \infty} \left| \frac{b^{(\nu-1)}}{b^{(\nu)}} \right|, \quad (52)$$

if this limit exists. Therefore, we determine the phase boundary  $(J/U)_{\text{pb}}$  by plotting the ratios  $\alpha_2^{(\nu-1)}/\alpha_2^{(\nu)}$  for orders  $\nu=1$  to  $8$  vs  $1/\nu$ , and by extrapolating to  $\nu=\infty$  by means of a linear fit. Figure 17 illustrates this scheme for dimensionalities  $d=2, 3, 5$ , and  $10$ , assuming unit filling. Note that the slope of the straight fitting lines decreases with increasing dimensionality, signaling the approach to the strictly geometric series present for  $d=\infty$ .

This method of extrapolation also provides a reliable estimate of the systematic error. If we employ different selec-

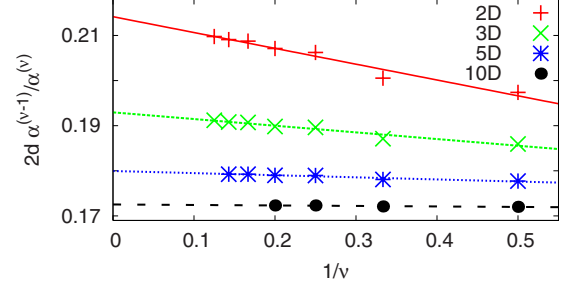


FIG. 17. (Color online) Extrapolation scheme for determining the phase boundary: The ratios  $\alpha_2^{(\nu-1)}/\alpha_2^{(\nu)}$  are plotted vs  $1/\nu$ , and extrapolated linearly to  $1/\nu=0$ . Data are given for dimensionalities  $d=2, 3, 5$ , and  $10$ , and chemical potential  $\mu/U=0.5$ . Observe that the slope decreases with increasing dimensionality.

tions of coefficients  $\alpha_2^{(\nu)}$ , such as those with  $\nu=2$  to  $8$  or  $\nu=3$  to  $8$ , we obtain very similar values for the phase boundary, thus confirming the high fidelity of our data. This is shown in Table III, which lists raw data for the critical hopping strengths  $(J/U)_c$ , marking the position of the tip of the respective Mott lobe. For the 2D system we thus estimate the overall relative error to be smaller than 2%, while it is smaller than 1% for the 3D model, and reduced still further in the four-dimensional case. The comparison of our results with recent data for  $g=1$  obtained by QMC methods<sup>18,19</sup> shows a remarkable agreement. Only close to the tip of the lobes small deviations are visible, as revealed by the inset of Fig. 18 for  $d=3$ . A similar comparison for  $d=2$  can be found in Ref. 25. The higher the filling factor, the more pronounced the model's approximate particle-hole symmetry<sup>2</sup> becomes, which renders the Mott lobes symmetric with respect to the chemical potential, such that the critical chemical potential approaches  $(\mu/U)_c = g - 0.5$  for high  $g$  (see Fig. 18). Interestingly, when multiplying the critical hopping parameters  $(J/U)_c$  for fixed dimensionality  $d$  and varying  $g$ , as listed in Table IV, by  $\sqrt{g(g+1)}$ , all data fall within a quite narrow range, as witnessed by Fig. 19.

We point out that the calculation of the phase boundary for  $d=1$  requires further considerations because of a re-entrance phenomenon:<sup>12</sup> For certain values of the chemical potential the transition from the Mott insulator to the superfluid in the 1D system is followed by another transition back to the insulator phase upon increasing  $J/U$ , before the super-

TABLE III. Critical values of the hopping parameter  $(J/U)_c$  for dimensionalities  $d=2, 3$ , and  $4$ , and filling factor  $g=1$ . These data were obtained from linear fits to coefficients from different orders  $\nu$ , as stated in the left column.

| $\nu$ | $(J/U)_c$                 |                           |                           |
|-------|---------------------------|---------------------------|---------------------------|
|       | $d=2$                     | $d=3$                     | $d=4$                     |
| 1–8   | $5.9093 \times 10^{-002}$ | $3.4068 \times 10^{-002}$ | $2.4131 \times 10^{-002}$ |
| 2–8   | $5.9853 \times 10^{-002}$ | $3.4248 \times 10^{-002}$ | $2.4189 \times 10^{-002}$ |
| 3–8   | $5.9403 \times 10^{-002}$ | $3.4092 \times 10^{-002}$ | $2.4107 \times 10^{-002}$ |
| 4–8   | $5.9846 \times 10^{-002}$ | $3.4255 \times 10^{-002}$ | $2.4163 \times 10^{-002}$ |
| 5–8   | $5.9482 \times 10^{-002}$ | $3.4080 \times 10^{-002}$ | $2.4093 \times 10^{-002}$ |

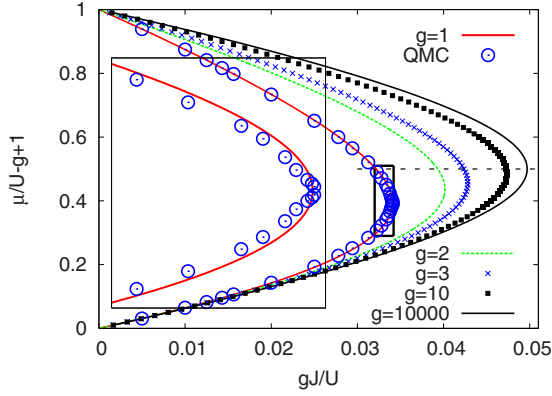


FIG. 18. (Color online) Mott lobes for  $d=3$  and various filling factors  $g$ . The dashed line marks the limit  $(\mu/U)_c = g - 0.5$  attained for high  $g$ . For  $g=1$ , QMC data (Ref. 18) are included. The inset magnifies the tip of the lobe belonging to unit filling.

fluid phase is reached again. Thus, for one value of  $\mu/U$  there then exist three phase-bounding values of  $J/U$ , which cannot immediately be extracted with our present procedure.

#### D. Approaching the mean-field limit

Although of lesser experimental relevance, it is still interesting to investigate systems with dimensionality  $d > 3$ , in order to study the convergence toward the mean-field limit. For higher  $d$  it becomes harder to obtain the necessary diagrams, and their weight factors. Nonetheless, we are able to treat systems of arbitrary dimensionality at least up to order  $\nu=4$  in the tunneling parameter  $J/U$  because the corresponding weight factors can still be figured out by combinatorial reasoning. Despite this relatively low order the precision of

TABLE IV. Critical values  $(\mu/U)_c$  and  $(J/U)_c$  for various filling factors  $g$ . For locating the tip of the respective Mott lobe,  $\mu/U$  has been varied in steps of 0.001. Relative errors of  $(J/U)_c$  are less than 1% for  $d=3$ , and less than 2% for  $d=2$ .

| $g$   | $d=2$       |                          | $d=3$       |                          |
|-------|-------------|--------------------------|-------------|--------------------------|
|       | $(\mu/U)_c$ | $(J/U)_c$                | $(\mu/U)_c$ | $(J/U)_c$                |
| 1     | 0.376       | $5.909 \times 10^{-002}$ | 0.393       | $3.407 \times 10^{-002}$ |
| 2     | 1.427       | $3.480 \times 10^{-002}$ | 1.437       | $2.007 \times 10^{-002}$ |
| 3     | 2.448       | $2.473 \times 10^{-002}$ | 2.455       | $1.427 \times 10^{-002}$ |
| 4     | 3.460       | $1.920 \times 10^{-002}$ | 3.465       | $1.108 \times 10^{-002}$ |
| 5     | 4.470       | $1.569 \times 10^{-002}$ | 4.472       | $9.055 \times 10^{-003}$ |
| 6     | 5.472       | $1.327 \times 10^{-002}$ | 5.476       | $7.657 \times 10^{-003}$ |
| 7     | 6.476       | $1.150 \times 10^{-002}$ | 6.479       | $6.634 \times 10^{-003}$ |
| 8     | 7.479       | $1.014 \times 10^{-002}$ | 7.482       | $5.852 \times 10^{-003}$ |
| 9     | 8.481       | $9.073 \times 10^{-003}$ | 8.484       | $5.235 \times 10^{-003}$ |
| 10    | 9.483       | $8.208 \times 10^{-003}$ | 9.485       | $4.736 \times 10^{-003}$ |
| 20    | 19.491      | $4.202 \times 10^{-003}$ | 19.492      | $2.425 \times 10^{-003}$ |
| 50    | 49.496      | $1.706 \times 10^{-003}$ | 49.497      | $9.842 \times 10^{-004}$ |
| 100   | 99.498      | $8.571 \times 10^{-004}$ | 99.498      | $4.946 \times 10^{-004}$ |
| 1000  | 999.500     | $8.609 \times 10^{-005}$ | 999.500     | $4.968 \times 10^{-005}$ |
| 10000 | 9999.500    | $8.613 \times 10^{-006}$ | 9999.500    | $4.970 \times 10^{-006}$ |

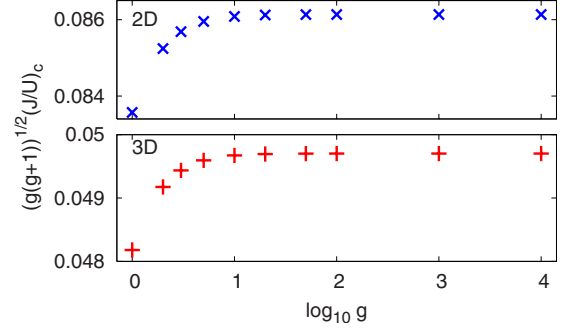


FIG. 19. (Color online) Scaled values  $\sqrt{g(g+1)}(J/U)_c$  of the critical hopping parameter vs filling factor  $g$  for  $d=2$  (upper panel) and  $d=3$  (lower panel). Observe the rather fine scale at the left margin.

the phase boundaries thus obtained is quite high for large  $d$  since the fluctuation of the ratio  $\alpha_2^{(\nu-1)}/\alpha_2^{(\nu)}$  decreases significantly with increasing  $d$ , as illustrated by Fig. 17. The resulting Mott lobes for unit filling are displayed in Fig. 20 for  $d=2, 3, 5, 10$ , and  $20$ , together with the mean-field phase boundary. In the limit  $d \rightarrow \infty$  the critical parameter  $(J/U)_c^{\text{mf}}$  can be deduced from Eq. (51), giving

$$2d(J/U)_c^{\text{mf}} = 2g + 1 - 2\sqrt{g(g+1)}, \quad (53)$$

which scales like  $1/g$  for large  $g$ . Hence, the approach to the mean-field limit can be well monitored by plotting the phase-bounding chemical potentials for each  $d$  vs  $2dJ/U$ , as in the main part of Fig. 20. While the curves agree fairly well with each other at the edges of the lobes even for low dimensionalities, larger deviations occur around the tips. The convergence to the mean-field phase boundary with increasing  $d$  is clearly visible. When plotting the scaled data  $2d\sqrt{g(g+1)}(J/U)_c$  for fixed  $g$  as functions of  $1/d$  in order to directly highlight the approach to infinite dimensionality, as done in the inset of Fig. 20 for  $g=1$  and  $g=10\,000$ , we obtain smooth curves aiming for  $1/d \rightarrow 0$  at the respective

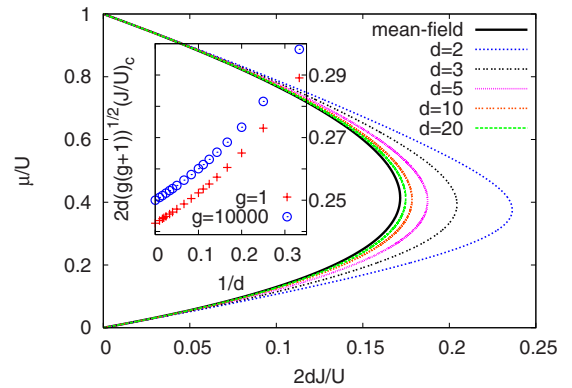


FIG. 20. (Color online) Phase diagram for dimensionalities  $d=2, 3, 5, 10$ , and  $20$ , together with the mean-field phase boundary, for  $g=1$ . With increasing dimensionality the data approach the mean-field prediction (51). In the inset the scaled critical hopping strength  $2d\sqrt{g(g+1)}(J/U)_c$  is plotted vs  $1/d$  for filling factors  $g=1$  (lower data set) and  $g=10\,000$  (upper data set).

mean-field result determined by Eq. (53). The scaled data belonging to different  $g$  fall into a remarkably narrow range; their relative separation amounts to about 3%. In fact, for any dimensionality  $d$  and any filling factor  $g$  the critical values computed in this work are fitted by

$$\left(\frac{J}{U}\right)_c = \left(\frac{J}{U}\right)_c^{\text{mf}} + \frac{0.13}{\sqrt{g(g+1)d^{2.5}}} \quad (54)$$

with an accuracy of about 1%, where  $(J/U)_c^{\text{mf}}$  follows from Eq. (53). Note that even for relatively high  $d$  the deviation from the mean-field prediction is not negligible. For example, even for  $d=10$  and  $g=1$  the value of  $(J/U)_c$  still exceeds the mean-field limit by about 4%.

## VI. CONCLUSION AND OUTLOOK

The essence of the high-order process-chain approach is captured by the example given in Sec. III A: On the one hand, one has to generate the Kato terms, as dictated by the perturbation series (8). This step is universal, and thus has to be done only once for all kinds of perturbative calculations. On the other hand, one has to construct all the diagrams pertaining to the particular observable under study, and their weight factors. These diagrams then are worked out in a Cinderella-type fashion: Each permutation of the processes constituting a diagram has to be compared to the pattern of intermediate states provided by the Kato terms; the matching permutations are evaluated, the others discarded. The bottlenecks of this scheme are the generation of the diagrams, which poses nontrivial combinatorial tasks in higher orders, and the factorial growth of the number of permutations with the order of perturbation theory. While it might be feasible to optimize diagram generation with the help of specifically adapted routines, the explosive growth of the number of permutations currently appears to limit straightforward numeri-

cal applications of this algorithm to about the 12th order.

But still, this could open up substantial possibilities for the further analysis of strongly correlated quantum many-body systems. This suggestion is underlined not only by our calculations of the various ground-state correlation functions for the homogeneous Bose-Hubbard model in Sec. IV, but also by the comprehensive determination of its phase diagram in Sec. V. The entire set of all dimensionalities  $d \geq 2$  and all filling factors  $g$  has been covered by a single approach, giving excellent agreement with previous findings in those cases for which accurate calculations had been performed before. In particular, our phase boundary for  $d=3$  and  $g=1$  virtually coincides with the result of a quite recent scaling analysis.<sup>10</sup>

The conceptual ease with which these results have been obtained here suggests that the process-chain approach<sup>20</sup> should also turn out useful for the theoretical investigation of other systems which so far are less well understood. We expect our strategy to work with similar success for different types of lattices, such as triangular or hexagonal ones, for ladder systems,<sup>36</sup> and for lattices with a superstructure, such as recently considered in Ref. 37.

## ACKNOWLEDGMENTS

We thank M. Langemeyer and V. Steenhoff for important help with the generation of high-order Kato terms, and B. Capogrosso-Sansone for providing the QMC data (Refs. 18 and 19). Computer power was obtained from the GOLEM I cluster of the Universität Oldenburg. N.T. acknowledges support from the Studienstiftung des deutschen Volkes. A.E. thanks M. Lewenstein for kind hospitality at ICFO-Institut de Ciències Fotòniques and acknowledges a Feodor Lynen research grant from the Alexander von Humboldt foundation, as well as support by the Spanish MEC [Grants No. FIS2008-00784 (TOQATA) and No. FIS2007-29996-E (ESF-EUROQUAM project FERMIX)]. This work was further supported by the Deutsche Forschungsgemeinschaft.

## APPENDIX A: NUMBER OF DIAGRAMS

TABLE V. Number of diagrams encountered to  $\nu$ th order in the tunneling coupling  $J/U$  when calculating the quantities considered in Sec. IV for the 3D Bose-Hubbard model. An obvious shorthand notation is used here for the lattice vectors introduced in Eq. (32), such that  $C(s)=C([s,0,0])$  and  $D(t,t)=D([t,t,0])$ .

| $\nu$       | 0 | 1 | 2 | 3 | 4 | 5  | 6  | 7  | 8   | 9   | 10   |
|-------------|---|---|---|---|---|----|----|----|-----|-----|------|
| $E$         |   |   | 1 |   | 3 |    | 7  |    | 29  |     | 127  |
| $C(1)$      |   | 1 |   | 3 |   | 10 |    | 50 |     | 281 |      |
| $C(2)$      |   |   | 1 |   | 3 |    | 15 |    | 102 |     | 795  |
| $C(3)$      |   |   |   | 1 |   | 3  |    | 18 |     | 102 |      |
| $C(4)$      |   |   |   |   | 1 |    | 3  |    | 19  |     | 151  |
| $C(1,1)$    |   |   | 1 |   | 3 |    | 17 |    | 126 |     | 1051 |
| $C(2,2)$    |   |   |   |   | 1 |    | 3  |    | 21  |     | 190  |
| $D(1)$      | 1 |   | 2 |   | 8 |    | 40 |    | 250 |     |      |
| $D(2)$      | 1 |   | 1 |   | 6 |    | 28 |    | 194 |     |      |
| $D(3)$      | 1 |   | 1 |   | 5 |    | 23 |    | 144 |     |      |
| $D(1,1)$    | 1 |   | 1 |   | 7 |    | 32 |    | 227 |     |      |
| $D(2,2)$    | 1 |   | 1 |   | 5 |    | 22 |    | 140 |     |      |
| $\hat{n}^2$ | 1 |   | 1 |   | 4 |    | 18 |    | 106 |     | 697  |

APPENDIX B: POSITIVITY OF  $c_4$ 

The method of the effective potential outlined in Sec. V A crucially requires that the coefficient of  $|\psi|^4$  in Eq. (43), and hence  $c_4$ , be positive. For evaluating  $c_4$  within the process-chain approach, we have to construct diagrams containing exactly two annihilation and two creation processes. To zeroth order in  $J/U$  (fourth order of the perturbation series), one gets one diagram with two creations and two annihilations at the same site ( $\bullet\bullet \times \times$ ), leading to  $4!/(2!)^2=6$  permutations. Similar to Eq. (15), the corresponding Kato terms are  $\langle \mathbf{m} | VS^2 VS^0 VS^1 V | \mathbf{m} \rangle$  and  $\langle \mathbf{m} | VS^1 VS^1 VS^1 V | \mathbf{m} \rangle$ . The relevant energy denominators are as follows:

$$\text{One hole: } \Delta E_h = g - 1 - \mu/U,$$

$$\text{Two holes: } \Delta E_{hh} = 2g - 3 - 2\mu/U,$$

$$\text{One particle: } \Delta E_p = \mu/U - g,$$

$$\text{Two particles: } \Delta E_{pp} = 2\mu/U - (2g + 1).$$

All these energy differences are negative, with

$$\begin{aligned} \Delta E_h &> \Delta E_{hh}, & \Delta E_p &> \Delta E_{pp}, \\ \Delta E_h &> \Delta E_{pp}, & \Delta E_p &> \Delta E_{hh}, \end{aligned} \quad (\text{B1})$$

as follows from  $g-1 < \mu/U < g$ . The combination of all contributions then yields

$$\begin{aligned} c_4^{(0)} &= \frac{g+1}{(\Delta E_p)^2} \left[ \frac{g+2}{\Delta E_{pp}} - \frac{g+1}{\Delta E_p} - \frac{g}{\Delta E_h} \right] \\ &+ \frac{g}{(\Delta E_h)^2} \left[ \frac{g-1}{\Delta E_{hh}} - \frac{g+1}{\Delta E_p} - \frac{g}{\Delta E_h} \right]. \end{aligned} \quad (\text{B2})$$

Since according to the above relations (B1) both factors in square brackets are positive, the coefficient  $c_4$  is manifestly positive to zeroth order in the tunneling parameter  $J/U$ . We have investigated higher orders in  $J/U$  numerically, and obtained only positive contributions  $\alpha_4^{(v)}$ .

\*teichmann@theorie.physik.uni-oldenburg.de

<sup>1</sup>M. Greiner, O. Mandel, T. Esslinger, T. W. Hänsch, and I. Bloch, *Nature (London)* **415**, 39 (2002).

<sup>2</sup>S. Sachdev, *Quantum Phase Transitions* (Cambridge University Press, Cambridge, England, 1999).

<sup>3</sup>D. Jaksch, C. Bruder, J. I. Cirac, C. W. Gardiner, and P. Zoller, *Phys. Rev. Lett.* **81**, 3108 (1998).

<sup>4</sup>I. Bloch, J. Dalibard, and W. Zwerger, *Rev. Mod. Phys.* **80**, 885 (2008).

<sup>5</sup>T. Stöferle, H. Moritz, C. Schori, M. Köhl, and T. Esslinger, *Phys. Rev. Lett.* **92**, 130403 (2004).

<sup>6</sup>I. B. Spielman, W. D. Phillips, and J. V. Porto, *Phys. Rev. Lett.* **98**, 080404 (2007).

<sup>7</sup>M. P. A. Fisher, P. B. Weichman, G. Grinstein, and D. S. Fisher, *Phys. Rev. B* **40**, 546 (1989).

<sup>8</sup>J. K. Freericks and H. Monien, *Phys. Rev. B* **53**, 2691 (1996).

<sup>9</sup>N. Elstner and H. Monien, *Phys. Rev. B* **59**, 12184 (1999).

<sup>10</sup>J. V. Freericks, H. R. Krishnamurthy, Y. Kato, N. Kawashima, and N. Trivedi, *Phys. Rev. A* **79**, 053631 (2009).

<sup>11</sup>T. P. Polak and T. K. Kopeć, *J. Phys. B* **42**, 095302 (2009).

<sup>12</sup>T. D. Kühner and H. Monien, *Phys. Rev. B* **58**, R14741 (1998).

<sup>13</sup>S. Rapsch, U. Schollwöck, and W. Zwerger, *Europhys. Lett.* **46**, 559 (1999).

<sup>14</sup>C. Kollath, U. Schollwöck, J. von Delft, and W. Zwerger, *Phys. Rev. A* **69**, 031601(R) (2004).

<sup>15</sup>C. Kollath, A. M. Läuchli, and E. Altman, *Phys. Rev. Lett.* **98**, 180601 (2007).

<sup>16</sup>G. G. Batrouni and R. T. Scalettar, *Phys. Rev. B* **46**, 9051 (1992).

<sup>17</sup>S. Wessel, F. Alet, M. Troyer, and G. G. Batrouni, *Phys. Rev. A* **70**, 053615 (2004).

<sup>18</sup>B. Capogrosso-Sansone, N. V. Prokof'ev, and B. V. Svistunov, *Phys. Rev. B* **75**, 134302 (2007).

<sup>19</sup>B. Capogrosso-Sansone, Ş. G. Söyler, N. Prokof'ev, and B. Svistunov, *Phys. Rev. A* **77**, 015602 (2008).

<sup>20</sup>A. Eckardt, *Phys. Rev. B* **79**, 195131 (2009).

<sup>21</sup>T. Kato, *Prog. Theor. Phys.* **4**, 514 (1949).

<sup>22</sup>B. Damski and J. Zakrzewski, *Phys. Rev. A* **74**, 043609 (2006).

<sup>23</sup>J. W. Negele and H. Orland, *Quantum Many-Particle Systems* (Westview, Reading, MA, 1998).

<sup>24</sup>F. E. A. dos Santos and A. Pelster, *Phys. Rev. A* **79**, 013614 (2009).

<sup>25</sup>N. Teichmann, D. Hinrichs, M. Holthaus, and A. Eckardt, *Phys. Rev. B* **79**, 100503(R) (2009).

<sup>26</sup>W. Zwerger, *J. Opt. B: Quantum Semiclassical Opt.* **5**, S9 (2003).

<sup>27</sup>D. J. Boers, B. Goedeke, D. Hinrichs, and M. Holthaus, *Phys. Rev. A* **75**, 063404 (2007).

<sup>28</sup>A. Messiah, *Quantum Mechanics* (Wiley, New York, 1966), Vol. 2.

<sup>29</sup>G. Baym, *Lectures on Quantum Mechanics* (Benjamin, Menlo Park, 1969).

<sup>30</sup>M. P. Gelfand, R. R. P. Singh, and D. A. Huse, *J. Stat. Phys.* **59**, 1093 (1990).

<sup>31</sup>F. Gerbier, A. Widera, S. Fölling, O. Mandel, T. Gericke, and I. Bloch, *Phys. Rev. A* **72**, 053606 (2005).

<sup>32</sup>A. Hoffmann and A. Pelster, *Phys. Rev. A* **79**, 053623 (2009).

<sup>33</sup>L. D. Landau and E. M. Lifschitz, *Statistical Physics, Part I (Course of Theoretical Physics, Vol. 5)* (Butterworths, Oxford, 1996).

<sup>34</sup>H. Kleinert, *Path Integrals in Quantum Mechanics, Statistics, Polymer Physics, and Financial Markets* (World Scientific, Singapore, 2006).

<sup>35</sup>E. T. Whittaker and G. N. Watson, *A Course of Modern Analysis* (Cambridge University Press, Cambridge, United Kingdom, 2000).

<sup>36</sup>P. Donohue and T. Giamarchi, *Phys. Rev. B* **63**, 180508(R) (2001).

<sup>37</sup>P. Barmettler, A. M. Rey, E. Demler, M. D. Lukin, I. Bloch, and V. Gritsev, *Phys. Rev. A* **78**, 012330 (2008).